Parameter Estimation and Tissue Segmentation from Multispectral MR Images

Zhengrong Liang, James R. MacFall, and Donald P. Harrington

Abstract— **A statistical method is developed to classify tissue types and to segment the corresponding tissue regions from relaxation time T_1, T_2, and proton density P_D weighted magnetic resonance images. The method assumes that the distribution of image intensities associated with each tissue type can be expressed as a multivariate likelihood function of three weighted signal intensity values (T_1, T_2, P_D) at each location within that tissue regions. The method further assumes that the underlying tissue regions are piecewise contiguous and can be characterized by a Markov random field prior. In classifying the tissue types, the method models the likelihood of realizing the images as a finite multivariate-mixture function. The class parameters associated with the tissue types (i.e., the weighted intensity means, variances and correlation coefficients of the multivariate function, as well as the number of voxels within regions of the tissue types) are estimated by maximum likelihood. The estimation fits the class parameters to the image data via the expectation-maximization algorithm. The number of classes associated with the tissue types is determined by the information criterion of minimum description length. The method segments the tissue regions, given the estimated class parameters, by maximum *a posteriori* probability. The prior is constructed by the tissue-region membership of the first- and second-order neighborhood. The method is tested by a few sets of T_1, T_2, and P_D weighted images of the brain acquired with a 1.5 Tesla whole body scanner. The number of classes and the asso ciated class parameters are automatically estimated. The regions of different brain tissues are satisfactorily segmented.**

I. Introduction

THE PURPOSES of segmenting magnetic resonance (MR) images are: (1) to quantify the volume sizes of different tissue types within the body, and (2) to visualize the tissue structures in three dimensions. The quantified tissue volumes from a number of similar patients reflect the pathological information about the disorder that the patients have [1]–[5]. For example, clinical studies in neuroradiology frequently use the measured volumes of some tissue types from the similar patients to obtain the information about the neuropathology and the neuropsychiatric and neuropsychological functions. Accurate measurement of the tissue volumes provides an effective mean in diagnosing the disorders. The tissue volumes determined in a time period contain the pathological information about that tissue [4]–[7]. For instance, clinical studies in oncology usually use the degree and duration of tumor shrinkage to judge the benefits of the therapy being evaluated. The complete disappearance of a tumor can translate into cure, and the lesser tumor responses may demonstrate biologic activity of the administered therapy. Accurate quantification of the tumor sizes provides a measure of the effectiveness of the treatment. The three dimensional (3D) display of different tissue structures facilitate greatly disease diagnosis, patient surgery and therapy [8]–[11]. For example, the shapes and sizes of the 3D displayed tissue structures will benefit a physician's diagnosis of the disorders and a surgeon's operations on the patient. A radiation therapist can practise a few treatment plannings on the display to optimize a maximal dose to the tumor with minimal radiation to the surrounding normal tissues.

The advantage of using MR images for 3D tissue segmentation and display is, as noted in a few reports published previously [12]–[17], the multispectral characteristics of MR images with relaxation times (i.e., T_1 and T_2) and proton density (i.e., P_D) information. With current fast MR imaging techniques, a set of three images can be acquired rapidly as T_1, T_2, and P_D weighted[1], respectively [18]–[26]. Since the three images are strongly correlated (or spatially registered) over the patient space, the information extracted by means of image processing from the images together is obviously more valuable than that extracted from each image individually [27]–[29], and is also expected to be more valuable than that obtained by simply adding the results from the three images respectively [12]. Therefore, a tissue segmentation from the three MR images is expected to produce more accurate 3D reconstruction and visualization than the segmentation obtained from each image individually or from the addition of the three images' segmentations.

In clinical applications, one of the major obstacles in 3D volume reconstruction and visualization of tissue structures from MR images is the difficulty in automating the segmentation of different tissue regions. Those previously reported supervised segmentation methods need intensive user interaction and so have the limitation in automating the segmentation [9]–[11], [13], [14], [17], [30]–[32]. Although the unsupervised segmentation approaches [12], [15], [16], [31]–[41] can essentially overcome this limitation, these ap-

Manuscript received September 23, 1992; revised April 20, 1993, November 25, 1993, and January 15, 1994. This work was supported by Grant #HL44194, awarded by the National Heart, Lung, and Blood Institute. The associate editor responsible for recommending this paper and coordinating its review was M. W. Vannier.

Z. Liang and D. P. Harrington are with the Department of Radiology, SUNY at Stony Brook, Stony Brook, NY 11794 USA; e-mail jzliang@ccmail.sunysb.edu.

J. R. MacFall is with the Duke University Medical Center, Durham, NC 27710 USA.

IEEE Log Number 9403433.

[1] It is noted that a T_1 weighted image is the image which is usually acquired using short T_R (or repetition time of a pulse sequence) and T_E (or spin-echo delay time). Similarly, a T_2 weighted image is acquired using relatively long T_R and T_E, and a P_D weighted image with long T_R and short T_E.

proaches usually require the estimate of the Gaussian Markov random field (MRF) parameters, the hierarchical parameters, or the model adjustable parameters. The estimation can be very difficult [27], [37], [38], [41], [42]. Further research on the track of unsupervised or automatic approach to tissue segmentation is necessary [32], [35], [38]. Great research effort has recently been devoted to develop automatic approaches as reported in the review articles [32], [43].

This paper describes a statistical automatic method. The method first classifies the tissue types (or estimates the class parameters associated with the tissue types) by maximum likelihood (ML) fitting the image data [44]–[46]. Then the method determines the optimal number of classes from the image data using information criteria [47]–[49]. Finally the method segments the tissue regions, given the estimated number of classes and the associated class parameters, by maximum *a posteriori* probability (MAP), where a MRF prior is assumed for the underlying tissue regions [28], [50], [51].

Since MR images have a spatial resolution at the range of the voxel size, the correlation of image intensities among nearby voxels may be weaker than that among the three images at a voxel. The method ignores the correlation of image intensities among nearby voxels and models the correlation of the three image intensities for each tissue type k as a multivariate likelihood function at each location (or a voxel) within that tissue regions [4], [14], [52]:

$$p_k(Y_i \mid \theta_k) = (2\pi)^{-3/2} \mid \chi_k \mid^{-1/2} \times \exp\left[-(1/2)(Y_i - \mathbf{u}_k)^\tau \chi_k^{-1}(Y_i - \mathbf{u}_k)\right] \quad (1)$$

where $Y_i = \{Y_{il}\}_{l=1}^3$ represents the data (or image intensity) vector of three elements (T_1, T_2, P_D) at location i over the voxel array of I voxels and $\{Y_{il}\}_{i=1}^I$ refers to a single image l. The notation θ_k associated with tissue type k stands for the vector $(\mathbf{u}_k, \chi_k)$, where $\mathbf{u}_k = \{\mu_{kl}\}_{k=1}^K$ and K is the number of tissue types or classes. In estimating the class parameters $(\mathbf{u}_k, \chi_k)$ from the image data $\{Y_i\}_{i=1}^I$, θ_k will be defined as the label of the vector $(\mathbf{u}_k, \chi_k)$, while in segmenting the tissue regions over the voxel array, θ_k will be referred as to the label of tissue type k. The parameter μ_{kl} is the intensity mean associated with class k and single image l. The parameter χ_k is the covariance (positive-definite symmetric) matrix associated with class k, and its three diagonal elements represent the intensity variances and the three off-diagonal elements are related to the correlation coefficients of the three images. The symbol τ stands for matrix transposition. If the three images are not correlated for each class k, the off-diagonal elements of χ_k will be zero, and (1) then becomes the product of three Gaussian functions. Each of the Gaussian functions is specified by its mean and variance. For segmentation from a single image, i.e., $l = 1$, $\mathbf{u}_k$ becomes the mean μ_k and χ_k the variance σ_k^2 for class k, determined by that image [29], [46].

As defined above θ_k will, in describing tissue segmentation, be referred as to the label of tissue type k. The labels are usually assigned as integers or colors for computer display. For example, $\Theta = \{\theta_k = k\}_{k=1}^K$, where integer 1 may be the label of skull bone for brain imaging, integer 2 the label of skull marrow, and integer K the label of cerebral spinal flow (CSF). If a voxel, say voxel i, is labeled by θ_k (or integer k), the voxel then belongs to tissue type k on the voxel array. Notation $\theta_{i/k}$ will be used to represent the labels or tissue types of neighbors of voxel i. Let X_i be the label variable of voxel i, then $X_i = \theta_k$ means that voxel i is classified to tissue type k. Similarly, $X_{i/k} = \theta_{i/k}$ means that the neighbors of voxel i are recognized by their labels or membership.

Since the underlying tissue regions are usually assumed as piecewise contiguous, i.e., the labels of nearby voxels are strongly correlated, the method uses a MRF prior to consider this property [50], [51], [53]:

$$p(X_i = \theta_k \mid X_{i/k} = \theta_{i/k}) = \alpha^{-1} \exp[-U(X)/\beta] \quad (2)$$

where α is the normalization constant, β the prior parameter, and $U(X)$ the energy function specified by the neighborhood membership.

The method aims to find that segmentation of tissue regions over the voxel array which satisfies:

$$\{\max_{k \in K}\} p_k(Y_i \mid \theta_k) p(X_i = \theta_k \mid X_{i/k} = \theta_{i/k}). \quad (3)$$

The segmentation determined by (3) can be shown to be equivalent to the MAP solution under the assumption that the posteriori probability satisfies [53]:

$$p(X_i = \theta_k \mid \mathbf{Y}, X_{\neq i} = \theta_{\neq i}) \approx p_k(Y_i \mid \theta_k) p(X_i = \theta_k \mid X_{i/k} = \theta_{i/k}) \quad (4)$$

where $\mathbf{Y} = \{Y_i\}_{i=1}^I$, $X_{\neq i}$ refers to the labels of all voxels on the voxel array, excluding the label of voxel i, and $\theta_{\neq i}$ has the similar meanings.

II. Method

Automating the MAP segmentation of (4) requires the class parameters $\{\mathbf{u}_k, \chi_k\}$, the number of classes K, and the prior parameter β being determined without user interaction.

A. Parameter Estimation

In classifying the tissue types or classes, there is usually little prior information available, so we make as few assumptions about the tissue types as possible. It is appropriate to estimate the class parameters $\{\mathbf{u}_k, \chi_k, K\}$ by fitting the parameters to the image data with ML or least squares. The method assumes the independence of the data vectors $\{Y_i\}$ over the voxel array and uses a finite multivariate mixture as the likelihood of realizing the three images given the underlying tissue types [54], [55]:

$$g(\mathbf{Y} \mid W, \Theta) = \prod_{i=1}^{I} \sum_{k=1}^{K} w_k p_k(Y_i \mid \theta_k) \quad (5)$$

where w_k is the ratio of the number of voxels within class k and the total number of voxels (i.e., I), $W = \{w_k\}_{k=1}^K$, and $\sum_k w_k = 1$. The mixture, which is represented by the summation term of (5), specifies the distribution of each data vector Y_i over the K classes with different weights $\{w_k\}$. There are many numerical techniques which can be employed to perform the ML fitting for the class parameters

$\{\mathbf{u}_k, \chi_k, w_k\}$. The method estimates those parameters using the expectation-maximization (EM) algorithm [44]. Assuming a set of initial estimate $\{\mathbf{u}_k^{(0)}, \chi_k^{(0)}, w_k^{(0)}\}_{k=1}^K$, the ML-EM fitting algorithm is expressed as [45], [56]:

$$w_k^{n+1} = \frac{1}{I}\sum_i Z_{ik}^{(n)}, \qquad \mu_{kl}^{n+1} = \frac{\sum_i Z_{ik}^{(n)} Y_{il}}{\sum_i Z_{ik}^{(n)}} \tag{6}$$

$$(\chi_k)_{lm}^{n+1} = \frac{\sum_i Z_{ik}^{(n)}(Y_{il} - \mu_{kl}^{(n+1)})(Y_{im} - \mu_{km}^{(n+1)})}{\sum_i Z_{ik}^{(n)}} \tag{7}$$

where

$$Z_{ik}^{(n)} = \frac{w_k^{(n)} p_k(Y_i \mid \theta_k^{(n)})}{\sum_j w_j^{(n)} p_j(Y_i \mid \theta_j^{(n)})}, \quad \theta_k^{(n)} = \theta_k(\mathbf{u}_k^{(n)}, \chi_k^{(n)}). \tag{8}$$

The derivation of the fitting algorithm and the meaning of the intermediate result $Z_{ik}^{(n)}$ are detailed in [49].

The number of classes K is determined by information criterion of minimum description length (MDL) [47], [48]:

$$\mathrm{MDL}(K) = -\ln[L(\mathbf{Y} \mid W, \Theta)] + \lambda J \ln(I) \tag{9}$$

where $L(\mathbf{Y} \mid W, \Theta)$ is the maximum likelihood of $g(\mathbf{Y} \mid W, \Theta)$ with parameters $\{W, \Theta\}$ estimated by the ML-EM fitting algorithm; $J = 10K - 1$ is the number of free parameters in W and Θ (i.e., $3K$ parameters of $\mathbf{u}_k$, $6K$ parameters of χ_k, and $K-1$ parameters of W); and $\lambda = 5/2$ is a scale factor [49]. The procedure for estimating the class parameters or classifying the tissue types $\{\mathbf{u}_k, \chi_k, w_k\}_{k=1}^K$ has been described in detail [49].

Once the class parameters are estimated, the K classes will be labeled by $\{\theta_k\}_{k=1}^K$. The assignment of the labels over the voxel array is then performed by the MAP segmentation procedure of (4).

B. Image Segmentation

In segmenting the tissue regions over the voxel array by the MAP approach of (4), the *a priori* assumption that the tissue regions are piecewise contiguous may be valid. The MRF prior of (2) matches the *a priori* assumption nicely [50], [51], [53]. The method chooses the energy function $U(X)$ as proportional to the number of nearby voxels belonging to a class, or mathematically [14], [15], [28], [51]:

$$U(X) = \sum_r [1 - \delta(X_i - X_r)] + \sum_s [1 - \delta(X_i - X_s)]/\sqrt{\gamma} \tag{10}$$

for voxel i, where $\delta(0) = 1$ and $\delta(\neq 0) = 0$. The index r runs over the 6 first-order neighbors of voxel i and index s covers the 12 second-order neighbors with $\gamma = 2$. The energy function can be extended to include the 8 third-order neighbors with $\gamma = 3$, and so on. The prior parameter $\beta = 1.0$ is determined empirically based on prior experiences [49]. The value of β is relatively larger, as compared to those reported by other researchers [14], [15], [28]. A relatively larger β means to weight the prior information lower with respect to the data likelihood. The purpose of lowering the prior information is to avoid obtaining a segmentation which has a higher posteriori probability than the true tissue regions have. Further improvement in the segmentation is expected to be obtained by modifying the energy function $U(X)$ rather than decreasing the value of β for a segment with a posteriori probability higher than the true probability.

The segmentation is performed iteratively, where voxel i is assigned to a region of tissue type k at the $(n+1)$-th iteration by:

$$\{\max_{k \in K}\} p_k(Y_i \mid \theta_k) p(X_i^{(n+1)} = \theta_k \mid X_{i/k}^{(n)} = \theta_{i/k}) \tag{11}$$

where $X_{i/k}^{(n)}$ represents the neighborhood membership of voxel i at the nth iteration and the labels $\{\theta_k\}_{k=1}^K$, which are associated with the classes $\{\mathbf{u}_k, \chi_k\}_{k=1}^K$, have been given by the parameter estimation described previously. This iterative approach can be shown to be equivalent to that of iterative conditional modes for the MAP solution [53]. If the *a priori* piecewise continuous information about the tissue regions is ignored, i.e., setting the MRF term equal to one, (11) reduces to the ML segmentation algorithm which is noniterative [56].

The parameter estimation and the image segmentation are accomplished automatically by a computer and the results are reported below.

III. Results

In order to test the stability and robustness of the automatic method, the ML-EM fitting algorithm of . (6)–(8), the information criterion of (9) and the MAP segmentation algorithm of (11) were applied to three different sets of T_1, T_2, and P_D weighted images acquired from three different normal brains. The method was further applied to a set of T_1, T_2, and P_D weighted images containing pathologically altered tissues or tumors. It is noted that although the automatic method is presented in three dimensions, its performance was studied for 2D slice images because of computer memory limitation.

The images were acquired by a 1.5 Tesla GE whole body scanner. The acquisition matrix was 128 × 256 with 1 NEX. The matrix was interpolated into 256 × 256 by zero-filling before Fourier transform to reconstruct the images of 256×256 size. The field of view was 24×24 cm^2. The slices were 5 mm thick with 5 mm inter-slice space. A fixed receiver bandwidth (16 KHz) was used.

The T_1 weighted (or short T_R and T_E) images were acquired using saturation recovery (SR) sequences, and the T_2 weighted (or long T_R and T_E) and P_D weighted (or long T_R and short T_E) images were obtained by multiple spin-echo (SE) scans. The SR and SE pulse sequences are routinely used in clinical studies.

The first set of normal-brain images was acquired using: (1) $T_R = 500$ msec and $T_E = 20$ msec for the T_1 weighted image (as shown on the top left of Fig. 1); (2) $T_R = 2,500$ msec and $T_E = 80$ msec for the T_2 weighted image (as shown on the top right of that figure); and (3) $T_R = 2,500$ msec and $T_E = 30$ msec for the P_D weighted image (as shown on the bottom of Fig. 1). The second set of normal-brain images was acquired by the same T_R and T_E settings as described above for the first set of images. The third set of normal-brain images had:

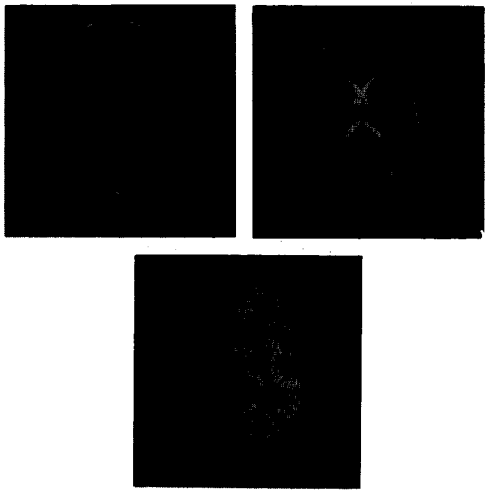

Fig. 1. The three slice images of T_1 (top left), T_2 (top right), and P_D (bottom) weighted. The T_1 weighted image was acquired with short T_R and T_E, the T_2 weighted image with long T_R and T_E, and the P_D weighted image with long T_R and short T_E.

TABLE I

w_k	w_1	w_2	w_3	w_4	w_5	w_6	w_7
image set 1	0.06	0.05	0.12	0.08	0.37	0.11	0.22
image set 2	0.06	0.04	0.11	0.08	0.36	0.09	0.27
image set 3	0.03	0.04	0.16	0.08	0.34	0.14	0.20

(1) $T_R = 1,000$ msec and $T_E = 20$ msec for the T_1 weighted image; (2) $T_R = 2,000$ msec and $T_E = 75$ msec for the T_2 weighted image; and (3) $T_R = 3,000$ msec and $T_E = 20$ msec for the P_D weighted image. Although the sizes of the three brains are quite different, the three sets of 2D images selected to test the segmentation algorithm have the similar tissue distribution (see Fig. 1).

The performance of parameter estimation for the three sets of images was consistent in terms of: (1) the same number of classes was determined $K = 7$, and (2) the relative pixel numbers $\{w_k\}$ in each corresponding class were similar for the three sets of data shown in Table I.

The three sets of segmented regions from the corresponding three sets of images were similar by visual judgement. The detailed description for segmenting one set of images is given below.

In order to test the hypothesis that the tissue segmentation from the multispectral images is better than that from a single image, each of the images in Fig. 1 was segmented, respectively, using the ML approach [i.e., setting the MRF term equal to one for (3)]. The ML approach is not iterative and does not have any adjustable parameters [56]. Each combination of two images in Fig. 1 was also segmented by that approach. The tissue segmentation from the three images together was better than the segmentations from the two-image combinations, and the later segmentations were better than those from each single image respectively. The judgement

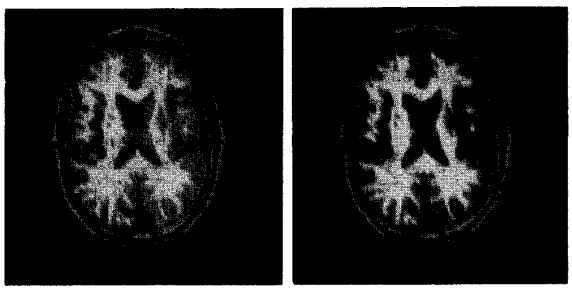

Fig. 2. The segmentations from the three images of Fig. 1 by the ML (left) and MAP (right) approaches.

was made by visual inspection. The segmentation from all three images contains all the features of the three images. However, the segmentations from two-image combinations, or single images, respectively, do not have the features contained in the image which is not used.

The ML segmentation from the three images together is shown on the left of Fig. 2. Although the segmentation has some small isolated spots (less than 4-pixel size) within the tissue regions, the ML approach is quite encouraging. The inclusion of the MRF prior for the MAP approach of (11) is then expected to remove those small isolated spots, since the prior imposes the piecewise continuous constraint on the segmentation. The segmentation from the three images together by the MAP approach is shown on the right of Fig. 2. The iterative MAP process was terminated after 3 iterations, since further iterations generated almost identical segmentations. The initial estimate for the MAP segmentation was the ML result as shown on the left of this figure. As compared with the ML segmentation, the MAP approach removed most of the small isolated spots within the tissue regions. However, some details near the edges of the tissue regions were sacrificed. Further improvement in reducing the spots while preserving the edge details can be obtained by the use of more suitable energy functions in the MRF prior of (2). To emphasize the contribution of the MRF constraint to the segmentation, the segmented tissue regions by the ML and MAP approaches as shown in Fig. 2 were extracted and are displayed in Figs. 3 and 4, respectively. The number of isolated small spots within each segmented region was reduced in the MAP segmentation of Fig. 4, as compared with the ML result of Fig. 3. For the task of quantifying the tissue volumes and displaying the tissue structures, the MAP segmentation provides an alternate approach that has the potential to reduce the spots while preserving the details, since the tissue regions are expected to be piecewise continuous and the small isolated spots will cause difficulty in volume quantification and in 3D display. Further studies are required to show the benefit of the MRF prior for tissue segmentation in three dimensions.

The top left of Fig. 4 shows the inner table of the skull, which contains the whole volume of the brain and the CSF space. The two spots on the top and inside the skull are the arteries. The two groups of spots each on the left and right and inside the skull are the arterial branches. The seven spots outside the skull (two on the left, two on the right, and three

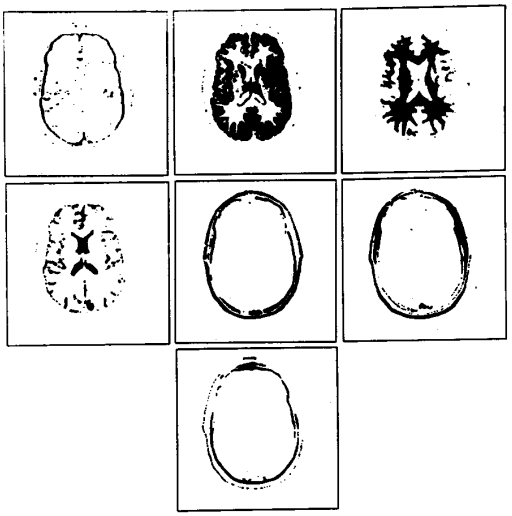

Fig. 3. The seven extracted classes from the ML segmentation on the left of Fig. 2. On the top left is the inner table of the skull, top middle the gray matter, and top right the white matter. On the middle left is the CSF space, middle center the subcutaneous fat and the diploic space, and middle right the temporalis muscle and the internal occipital protuberance. The bottom segment is the outer table of the skull and the skin.

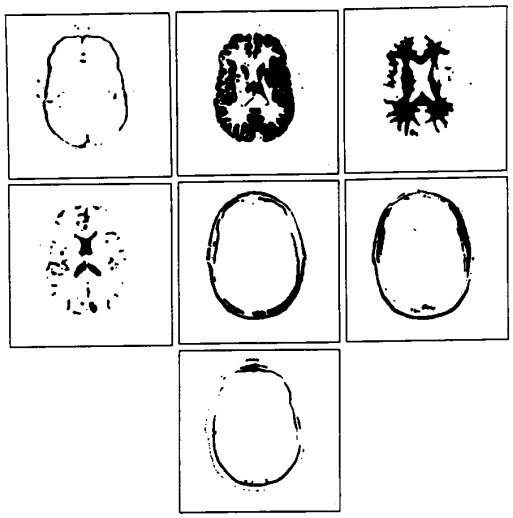

Fig. 4. The seven extracted classes from the MAP segmentation on the right of Fig. 2. The seven segments have the same meanings as those of Fig. 3.

on the top) are the blood vessels. The edge on the bottom right is broken. The MRF prior should be modified to avoid such edge breaking. On the top middle of Fig. 4 is the gray matter. The white matter is shown on the top right and the CSF space on the middle left. The four small spots outside the gray matter and the three small spots outside the white matter should be removed by modifying the MRF function. The segmented regions of inner table, CSF space, gray and white matters are the most important ones. The summation of the regions on the top middle and right of Fig. 4 gives the volume of the brain. The subtraction of the brain volume from the volume of the

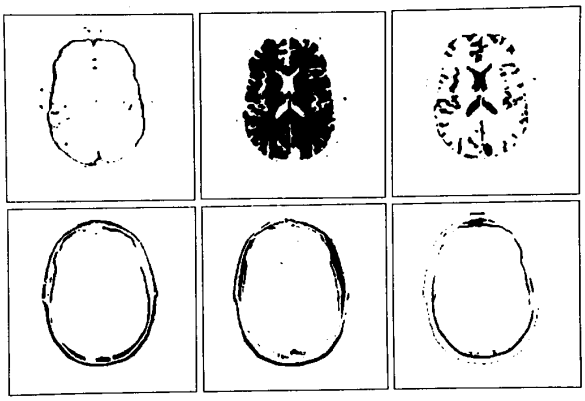

Fig. 5. The extracted regions from the MAP segmentation assuming six classes in the images.

top left regions results in the CSF space. The importance of quantifying the brain and CSF volumes is well known. For example, in atrophy, the CSF volume will increase. In the center of Fig. 4 are the subcutaneous fat and the diploic space. The region on the middle right mainly contains the temporalis muscle and the internal occipital protuberance. The small spot near the center is not expected and should be removed with a modification of the MRF prior. On the bottom of the figure are the outer table of the skull and the skin. Although the last three segments are mixtures of different tissue types due to the similar image-intensity variations of those tissue types, these regions do not contribute to the volume quantification and the 3D display of the brain tissues. By comparing the extracted regions of Fig. 4 with the three original images of Fig. 1, it can be seen that the regions having different image intensities were satisfactorily segmented, especially the brain tissues, the CSF space and the inner table of the skull were clearly identified. The seven different classes were automatically selected by the MDL criterion.

To see the benefit from the MDL criterion in selecting the number of classes K, the ML-EM fitting algorithm was performed to estimate the parameters when 6 and 8 classes were assumed in the images. The MAP segmentations from the estimated parameters of 6 and 8 classes are shown in Figs. 5 and 6, respectively. The MDL values for 6, 7, and 8 classes are: MDL(6) = 151890, MDL(7) = 149843, and MDL(8) = 150218. It is seen that the segmentation from the selected 7 classes is the optimal result. If the class number was "underestimated" by one, the white matter merged with the gray matter into a single class. When the class number was "overestimated" by one, the extra class as shown in the bottom middle of Fig. 6 appeared, which contains tissue types both inside and outside the skull and so is not needed.

In Table II, $\{\mu_{k1}\}$ and $\{\sigma_{k1}^2\}$ are the intensity means and variances associated with the T_1 weighted image, $\{\mu_{k2}\}$ and $\{\sigma_{k2}^2\}$ associated with the T_2 weighted image, and $\{\mu_{k3}\}$ and $\{\sigma_{k3}^2\}$ associated with the P_D weighted image. The correlation coefficients $\{\rho_{12}(k)\}$ are for the classes between the T_1 and T_2 weighted images, $\{\rho_{13}(k)\}$ for the T_1 and P_D weighted images, and $\{\rho_{23}(k)\}$ for the T_2 and P_D weighted images.

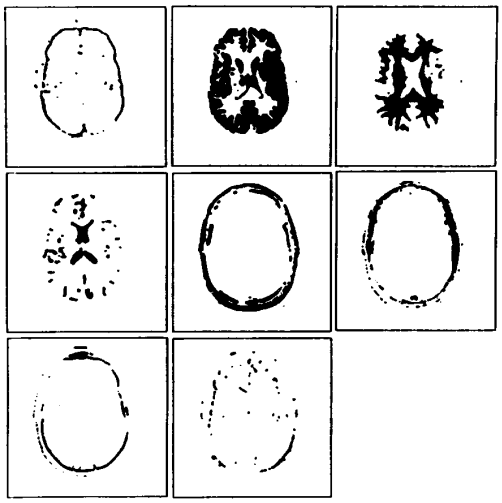

Fig. 6. The extracted regions from the MAP segmentation assuming eight classes in the images.

Fig. 7. The three slice images of T_1 (top left), T_2 (top right), and P_D (bottom) weighted, containing pathologic alterations. The T_1 weighted image is a Gd-enhanced scan.

TABLE II
INTENSITY MEANS, VARIANCES, AND CORRELATION COEFFICIENTS OF SELECTED SEVEN CLASSES

k	w_k	μ_{k1}	μ_{k2}	μ_{k3}	σ_{k1}^2	σ_{k2}^2	σ_{k3}^2	$\rho_{12}(k)$	$\rho_{13}(k)$	$\rho_{23}(k)$
1	0.06	1.50	1.00	2.48	1.09	0.48	2.37	0.55	0.38	0.74
2	0.05	4.96	8.06	10.17	6.91	10.46	17.62	0.22	0.27	0.95
3	0.12	5.30	3.25	8.01	3.19	1.90	4.74	0.43	0.42	0.79
4	0.08	6.53	12.92	15.00	2.55	6.39	0.92	-0.41	0.09	0.17
5	0.37	8.23	9.57	14.53	0.65	1.89	1.52	-0.52	-0.29	0.73
6	0.11	9.39	3.42	7.70	12.24	2.95	14.17	0.80	0.81	0.95
7	0.22	9.43	7.93	12.58	0.16	0.48	0.44	-0.12	0.26	0.49

The summation $\sum_k w_k \approx 1.0$ is expected. Class k=1 stands for the outer table of the skull and the skin, k =2 for the inner table of the skull, k=3 for the temporalis muscle and internal occipital protuberance, k=4 for the CSF space, k=5 for the gray matter, k=6 for the subcutaneous fat and the diploic space, and k=7 for the white matter. The estimated parameters of the seven classes are listed in Table II. The third and sixth classes of the T_2 and P_D weighted images have the similar intensity means, but those classes in the T_1 weighted image do not. (It is noted that the image data were first converted to real values and then scaled to the range of [0.0, 20.0] for the parameter estimation). The intensity means of the second and seventh classes in the T_2 weighted image are similar, but they are not in the T_1 and P_D weighted images. The similar result is seen for the second and third classes, as well as the sixth and seventh classes of the T_1 weighted image. This observation suggests that any tissue type which has distinct image-intensity distribution within any one of the three images will be identified, even it is not distinguishable within the other two images. Most of the variance parameters are different except for the first and seventh, as well as the third and fifth classes in the T_2 weighted image. The correlation of the three images for each class is shown by the correlation coefficients.

The automatical tissue segmentation from images of normal brains is very encouraging as demonstrated above. The performance of the automatic method for images of pathologically altered brain tissues is described below.

Fig. 7 shows the three T_1, T_2, and P_D weighted images containing a tumor. They were acquired by the same MR scanner with the same protocol settings as mentioned before. The top left is a T_1 weighted image with T_R = 500 msec and T_E = 30 msec. It was acquired after injection of Gd-DTPA (i.e., it is a Gd enhanced image). For tumor imaging, the contrast agent is routinely used. The top right is a T_2 weighted image with T_R = 2000 msec and T_E = 60 msec. The bottom one is a P_D weighted image with T_R = 3000 msec and T_E = 30 msec.

From the three images of Fig. 7, nine classes were determined. The segmented 9 classes by the MAP approach are shown in Fig. 8. The tumor and the surrounding edema were segmented as shown in the center and on the middle right of Fig. 8. The other seven segmented classes are somewhat similar to those as shown in Fig. 4. On the middle right of Fig. 8 is the enhanced tissue or the tumor periphery with Gd contrast. In the center of Fig. 8, the central isolated area is the tumor which is separated from the surrounding edema by the enhanced tissue. The tumor size and shape can be determined by the structure of the enhanced tissue. This tumor segmentation shows the advantage of using multispectral MR images for tumor quantification by the following evidence. Although the enhanced tissue is clearly seen in the T_1 weighted image, the edema and the tumor are not distinguishable from the white matter. Similarly, although the edema and the tumor are differentiated from the white matter in the T_2 and P_D weighted images, it is very difficult to trace the tumor on these two images. As compared to the tissue classification from normal-brain images, the tumor segmentation is much more difficult, since the segmentation is tumor type and stage dependent. The tumor, edema, scar tissue, and radiation

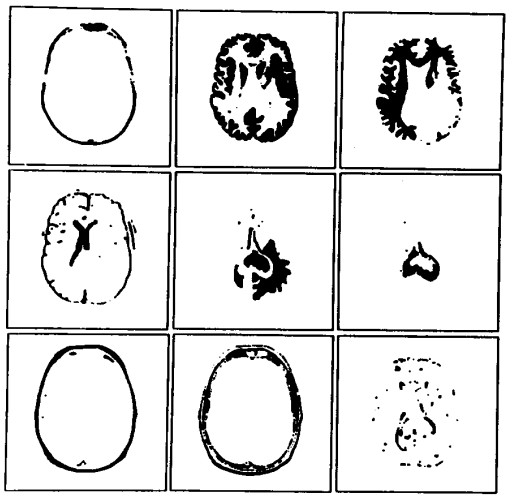

Fig. 8. The nine segmented classes using the MAP approach. The tumor and the surrounding tissues or edema are shown in the center and on the middle right. On the middle right is the enhanced tissue. In the center, the central isolated area is the tumor which is separated from the surrounding edema by the enhanced tissue.

induced necrosis have very similar intensities in the T_1, T_2, and P_D weighted images.

The computing programs for classifying the tissue types and segmenting the tissue regions were coded in Fortran language. The programs were executed on a HP/730 computer workstation. The parameter estimation took approximately 15 minutes and the image segmentation finished in less than one minute.

IV. Discussion

In presenting the MAP segmentation criterion of (3), the method considered: (1) the image-intensity correlation of the three images at a location within a same tissue type via the multivariate likelihood function of (1); and (2) the tissue-type correlation among nearby voxels via the MRF prior of (2). The likelihood function was formulated for each tissue type k and the prior was constructed based on the nearby voxel membership with respect to the class k. The segmentation criterion of (3) examines each data vector $Y_i = \{Y_{il}\}_{l=1}^{3}$ against the K determined classes and reviews each class membership $X_{i/k}$ (or the neighbors of voxel i) against the considered class k in order to label the voxel i appropriately. The image-intensity correlation among nearby voxels was ignored. The correlation may be considered as (1) within a single image $\{Y_{il}\}$ among nearby elements $\{Y_{jl}\}$ with $j = i \pm 1$, or (2) within the image vectors $\{Y_i\}$ among nearby vector elements $\{Y_{i\pm1}\}$. The inclusion of the first correlation form into (1) is an interesting topic and is worth for further investigation. The second approach to the correlation will make the parameter estimation very difficult and so will not be considered in the future.

In estimating the class parameters, the method assumed the independence of data vector $\{Y_i\}$ over the voxel array and did not make any assumption about the single-image intensity correlation $\{Y_{il}\}$. Modifying $p_k(Y_i \mid \theta_k)$ of (1) to include the single-image intensity correlation will not effect the analysis of the method, and probably the modification might cause the numerical calculation to be very complicated. Since the parameter estimation of (5)–(8) did not consider the correlation of the single-image intensities among neighborhood, a small object or a tumor could possibly be misclassified. Although a classification using pathologically altered image data with a relatively large tumor was performed, further studies for small tumors are needed.

In formulating the likelihood function of (1), the method assumed that the distribution of the single-image intensities $\{Y_{il}\}$ for each tissue type k follows a Gaussian function. In practical situations, due to the pathological condition of the tissue, the inhomogeneities of magnetic and/or radio frequency (RF) fields, the attenuation of RF within that tissue and other artifacts, the intensity distribution may not necessarily be a Gaussian for that tissue type. Although the functional form of the likelihood function does not affect the analysis of the method, accurately modeling the intensity distribution is necessary. The Gaussian model of (1) needs further validation using image data acquired in different situations. The precorrection procedure may be necessary [57].

In implementing the automatic method, the three images are chosen arbitrarily. Since the method can identify the tissue type if its image-intensity variation is distinct within any one of the three images, then the question of how to acquire the three or more images which differentiate the most interested tissues arises immediately. The three T_1, T_2, and P_D weighted images of Fig. 1 are, of course, a choice. Other acquisition protocols for the multispectral images are worth investigating.

It is noted that the presented studies using the limited number of image data and acquisition protocols are very preliminary. Further investigation by anthropomorphic phantom experiments for accuracy validation and by a large number of clinical scans for stability test is necessary.

V. Conclusion

A statistical method for tissue classification and segmentation from multispectral MR images of T_1, T_2, and P_D weighted was described and tested. The number of classes and the associated class parameters were consistently estimated. The tissue regions were satisfactorily segmented. The parameter estimation and the tissue segmentation were performed automatically by a computer. The parameter estimation can be improved by introducing *a priori* constraints for MAP solution, rather than ML estimate. The segmentation can be improved by modifying the energy function of the MRF prior. The weighted images acquired for the segmentation experiments can be used to compute the true T_1, T_2, and P_D images [58], [59]. This automatic approach can be applied to segment these computed intrinsic images [60]. Although the presented studies were performed for 2D images, the algorithms for classification and segmentation were derived for 3D situations and the implementation in three dimensions is straightforward.

The verification of the automatic method as shown above is qualitative. Quantitative validation on the accuracy and stability of the method needs further experimental studies using different acquisition protocols, realistic anthopomorphic phantoms, and a large number of clinical scans.

ACKNOWLEDGMENT

The authors appreciate Dr. T. Turkington, Dr. G. Gindi, and Dr. C. Roque for their assistance in preparing this manuscript.

REFERENCES

[1] C. R. Jack, F. W. Sharbrough, and C. K. Twomey, et al., "Temporal lobe seizures: lateralization with MR volume measurements of the hippocampal formation," *Radiology*, vol. 175, pp. 423–429, 1990.

[2] G. D. Cascino, C. R. Jack, and J. E. Parisi, et al., "Magnetic resonance imaging-based volume studies in temporal lobe epilepsy: Pathological correlations," *Ann. Neurology*, vol. 30, pp. 31–36, 1991.

[3] T. Lencz, G. McCarthy, and R. A. Bronen, et al., "Quantitative magnetic resonance imaging in temporal lobe epilepsy: Relationship to neuropathology and neuropsychological function," *Ann. Neurology*, vol. 31, pp. 629–637, 1992.

[4] M. I. Kohn, N. K. Tanna, and G. T. Herman, et al., "Analysis of brain and cerebrospinal fluid volumes with MR imaging, Part I. Methods, reliability, and validation," *Radiology*, vol. 178, pp. 115–122, 1991.

[5] N. K. Tanna, M. I. Kohn, and D. N. Horwich, et al., "Analysis of brain and cerebrospinal fluid volumes with MR imaging: Impact on PET data correlation for atrophy, Part II. Aging and Alzheimer dementia," *Radiology*, vol. 178, pp. 123–130, 1991.

[6] F. Miraldi, "Potential of NMR and PET for determining tumor metabolism," *Int. J. Radio. Oncol. Biol. Phys.*, vol. 12, pp. 1033–1039, 1986.

[7] S. A. Grossman and P. A. Burch, "Quantitation of tumor response to anti-neoplastic therapy," *Seminars in Oncology*, vol. 15, pp. 441–454, 1988.

[8] G. T. Herman, J. K. Udupa, and D. M. Kramer, et al., "The 3D display of NMR images," *Optical Engin.*, vol. 21, pp. 923–926, 1982.

[9] M. Bomans, K. H. Hohne, U. Tiede, and M. Riemer, "Three-dimensional segmentation of MR images of the head for 3D display," *IEEE Trans. Medical Imaging*, vol. 9 pp. 177–183, 1990.

[10] H. E. Cline, W. E. Lorensen, R. Kikinis, and F. Jolesz, "Three-dimensional segmentation of MR images of the head using probability and connectivity," *JCAT*, vol. 14, pp. 1037–1045, 1990.

[11] S. P. Raya, "Low-level segmentation of 3D MR brain images—A rule-based system," *IEEE Trans. Medical Imaging*, vol. 9, pp. 327–337, 1990.

[12] D. A. Ortendahl, N. M. Hylton, L. Kaufman, and L. E. Crooks, "Tissue characterization using intrinsic NMR parameters and a hierarchical processing algorithm," *IEEE Trans. Nuclr Sci.*, vol. 32, pp. 875–879, 1985.

[13] M. W. Vannier, R. L. Butterfield, and D. Jordan, et al., "Multispectral analysis of MR images," *Radiology*, vol. 154, pp. 221–224, 1985.

[14] H. S. Choi, D. R. Haynor, and Y. Kim, "Multivariate tissue classification of MR images for 3D volume reconstruction—A statistical approach," in *SPIE Med. Imag. III*, pp. 183–193, 1989.

[15] R. Leahy, T. Hebert, and R. Lee, "Applications of Markov random field models in medical imaging," in *Proc. IPMI*, vol. 11, pp. 1–14, 1989.

[16] M. Goldbach, W. Menhardt, and J. Stevens, "Multispectral tissue characterization in MR imaging using Bayesian estimation and Markov random fields," in *Proc. IEEE EMB*, vol. 13, pp. 62–63, 1991.

[17] R. P. Velthuizen, L. P. Clarke, L. O. Hall, and A. M. Bensaid, "Multispectral 3D MRI segmentation using knowledge based systems," *Med. Physics*, vol. 18, p. 623, 1991.

[18] I. R. Young, M. Burl, and G. M. Bydder, "Comparative Efficiency of different pulse sequences in MR imaging," *JCAT*, vol. 10, pp. 271–286, 1986.

[19] H. Iwaoka, T. Hirata, and H. Matsuura, "Optimal pulse sequences for magnetic resonance imaging—Computing accurate T_1, T_2, and proton density images," *IEEE Trans. Medical Imaging*, vol. 6, pp. 360–369, 1987.

[20] U. Klose, T. Nagele, M. Skalej, and W. Grodd, "Fast T_1- and T_2-weighted images using a modified snapshot FLASH technique," in *Proc. SMRM*, p. 1047, 1989.

[21] A. Haase, "Snapshot FLASH MRI: Applications to T_1, T_2, and chemical shift imaging," *Magn. Reson. Res.*, vol. 13, pp. 77–89, 1990.

[22] A. Holsinger and S. Riederer, "The importance of phase-encoding order in ultra-short T_R snapshot MR imaging," *Magn. Reson. Med.*, vol. 16, pp. 481–488, 1990.

[23] S. A. Mirowitz, J. K. Lee, and J. J. Brown, et al., "Rapid acquisition spin-echo (RASE) MR imaging: A new technique for reduction of artifacts and acquisition time," *Radiology*, vol. 175, pp. 131–135, 1990.

[24] F. Wehrli, *Fast-Scan Magnetic Resonance: Principles and Applications.* New York: Raven, 1990.

[25] M. S. Cohen and R. M. Weiskopf, "Ultrafast imaging," *Magn. Reson. Imag.*, vol. 9, pp. 1–37, 1991.

[26] E. M. Haacke, P. A. Wielopolski, and J. A. Tkach, "A comprehensive technical review of short T_R, fast, magnetic resonance imaging," *Rev. Mag. Res. Med.*, vol. 3, pp. 53–170, 1991.

[27] S. Lakshmanan and H. Derin, "Simultaneous parameter estimation and segmentation of Gibbs random fields using simulated annealing," *IEEE Trans. PAMI*, vol. 11, pp. 799–813, 1989.

[28] R. C. Dubes, A. K. Jain, S. G. Nadabar and C. C. Chen, "MRF model-based algorithms for image segmentation," in *Proc. IEEE ICPR*, pp. 808–814, 1990.

[29] T. Lei and W. Sewchand, "Statistical approach to X-Ray CT imaging and its applications in image analysis—Part II: A new stochastic model-based image segmentation technique for X-ray CT image," *IEEE Trans. Medical Imaging*, vol. 11, pp. 62–69, 1992.

[30] D. N. Kennedy, P. A. Filipek, and V. S. Caviness, "Anatomic Segmentation and volumetric calculations in nuclear MR imaging," *IEEE Trans. Medical Imaging*, vol. 8, pp. 1–7, 1989.

[31] A. M. Bensaid, L. O. Hall, L. P. Clarke, and R. P. Velthuizen, "MRI segmentation using supervised and unsupervised methods," in *Proc. IEEE EMB*, vol. 13, pp. 60–61, 1991.

[32] L. O. Hall, A. M. Bensaid, and L. P. Clarke, et al., "A comparison of neural network and fuzzy clustering techniques in segmenting MR images of the brain," *IEEE Trans. Neural Networks*, vol. 3, pp. 672–683, 1992.

[33] Z. Wu and R. Leahy, "Tissue classification in MR images using hierarchical segmentation," *Conf. Record NSS-MIC*, pp. 1410–1414, 1990.

[34] L. P. Clarke, "MR image segmentation using MLM and artificial neural nets," *Med. Physics*, vol. 18, p. 673, 1991.

[35] W. T. Katz and M. B. Merickel, "Automated segmentation of 3D MR images of the head," in *Proc. IEEE EMB*, vol. 13, pp. 297–298, 1991.

[36] J. W. Snell and M. B. Berickel, "Tissue labelling of MRI using recurrent artificial neural networks," in *Proc. IEEE EMB*, vol. 13, pp. 66–67, 1991.

[37] S. C. Amartur, D. Piraino, and Y. Takefuji, "Optimization neural networks for segmentation of MR images," *IEEE Trans. Medical Imaging*, vol. 11, pp. 215–220, 1992.

[38] G. Gerig, J. Martin, and R. Kikinis, et al., "Automating segmentation of dual-echo MR head data," in *Proc. IPMI*, vol. 12, pp. 175–187, 1992.

[39] S. D. Pinski, S. K. Rogers, and D. W. Ruck, et al., "Image segmentation using optical wavelets," in *SPIE Hybrid Image and Signal Proc. III*, vol. 1702, p. 11, 1992.

[40] A. Simmons, S. R. Arridge, G. S. Barker, and P. Tofts, "Segmentation of neuroanatomy in MR images," in *SPIE Med. Imag. VI*, vol. 1652, pp. 2–13, 1992.

[41] W. Snyder, A. Logenthiran, and P. Santago, et al., "Segmentation of MR images using mean field annealing," in *Proc. IPMI*, vol. 12, pp. 218–226, 1992.

[42] C. S. Won and H. Derin, "Maximum likelihood estimation of Gaussian Markov random field parameters," in *Proc. IEEE ICASSP*, pp. 1040–1043, 1988.

[43] J. C. Bezdek, L. O. Hall, and L. P. Clarke, "Review of MR image segmentation techniques using pattern recognition," *Med. Physics*, vol. 20, pp. 1033–1048, 1993.

[44] A. P. Dempster, N. M. Laird, and D. B. Rubin, "Maximum likelihood from incomplete data via the EM algorithm," *JRSS*, vol. 38B, pp. 1–38, 1977.

[45] R. A. Redner and H. F. Walker, "Mixture densities, maximum likelihood and the EM algorithm," *SIAM Rev.*, vol. 26, pp. 195–239, 1984.

[46] Z. Liang, R. J. Jaszczak, and R. E. Coleman, "On Reconstruction and segmentation of piecewise continuous images," in *Proc. IPMI*, vol. 12, pp. 94–104, 1991.

[47] J. Rissanen, "Modeling by shortest data description," *Automatica*, vol. 14, pp. 465–471, 1978.

[48] G. Schwarz, "Estimating the dimension of a model," *Ann. Statist.*, vol. 6, pp. 461–464, 1978.

[49] Z. Liang, R. J. Jaszczak, and R. E. Coleman, "Parameter estimation of finite mixtures using the EM algorithm and information criteria with

application to medical image processing," *IEEE Trans. Nucl. Sci.*, vol. 39, pp. 1126–1133, 1992.
[50] R. Kindermann and J. L. Snell, "Markov random fields and their applications," *Amer. Math. Soc.*, vol. 1, pp. 1–142, 1980.
[51] S. Geman and D. Geman, "Stochastic relaxation, Gibbs distributions, and the Bayesian restoration of images," *IEEE Trans. PAMI*, vol. 6, pp. 721–741, 1984.
[52] J. H. Wolfe, "Pattern clustering by multivariate mixture analysis," *Multivariate Behavioral Res.*, vol. 5, pp. 329–350, 1970.
[53] J. Besag, "On the statistical analysis of dirty pictures," *JRSS*, vol. 48B, pp. 259–302, 1986.
[54] B. S. Everitt and D. J. Hand, *Finite Mixture Distribution*. New York: Chapman and Hall, 1981.
[55] D. M. Titterington, A. F. M. Smith, and U. E. Makov, *Statistical Analysis of Finite Mixture Distributions*.New York: John Wiley & Sons, 1985.
[56] Z. Liang, "Tissue classification and segmentation of MR Images," *IEEE EMB Mag.*, vol. 12, pp. 81–85, 1993.
[57] B. M. Dawant, A. P. Zijdenbos, and R. A. Margolin, "Correction of intensity variations in MR images for computer-aided tissue classification," *IEEE Trans. Medical Imaging*, vol. 12, pp. 770–781, 1993.
[58] D. A. Ortendahl, N. M. Hylton, and L. Kaufman, et al., "Calculated NMR images," in *Proc. MR in Medicine*, pp. 272–273, 1983.
[59] J. R. MacFall, "Pulse sequence considerations for computed T_1, T_2, and spin density images," *Technology of NMR*, vol. 1, pp. 79–96, 1984.
[60] Z. Liang and J. R. MacFall, "Automatic tissue segmentation from computed intrinsic MR images," in *Proc. SMRM*, pp. 695, 1993.